Nano Research
2022, 15(1): 701–708
ISSN 1998-0124 CN 11-5974/O4
https://doi.org/10.1007/s12274-021-3550-5

Research Article

Flexible aqueous Ca-ion full battery with super-flat discharge voltage plateau

Panpan Wang[1], Hua Wang[2,3,4], Zhe Chen[2,3,4], Junwei Wu[4], Jingting Luo[5], and Yan Huang[2,3,4] (✉)

[1] School of Materials Science and Engineering, Shenzhen University, Shenzhen 518055, China
[2] State Key Laboratory of Advanced Welding and Joining, Harbin Institute of Technology, Shenzhen 518055, China
[3] Flexible Printed Electronic Technology Center, Harbin Institute of Technology, Shenzhen 518055, China
[4] School of Materials Science and Engineering, Harbin Institute of Technology, Shenzhen 518055, China
[5] College of Physics and Optoelectronic Engineering, Shenzhen University, Shenzhen 518055, China

Received: 18 March 2021 / **Revised:** 17 April 2021 / **Accepted:** 27 April 2021

ABSTRACT

Recently, multivalent metal-ion batteries have attracted considerable interests on the merits of their natural abundance and multi-electron redox property. However, the development of Ca-ion battery is still in their preliminary stage because of the lack of suitable electrode material. The Ca-storage performance of the existing materials is still unsatisfactory with low capacity, poor cyclic stability, as well as sloping discharge profiles, which cannot provide stable energy output. In this work, transition metal oxide Sn-doped In_2O_3 (ITO) has been explored as the aqueous Ca-ion battery anode, which could deliver a high discharge capacity of 71.2 mAh·g^{-1} with an ultra-flat discharge voltage plateau. The Ca storage mechanism was revealed to be reversible conversion reaction based on *ex-situ* X-ray diffraction (XRD), X-ray photoelectron spectroscopy (XPS), and transmission electron microscopy (TEM) characterizations. A flexible aqueous Ca-ion battery was subsequently assembled with zinc hexacyanoferrate (ZnHCF) cathode and ITO anode sandwiched by hydrogel electrolyte, which could deliver a high specific capacity of 75.3 mAh·g^{-1} at 0.4 A·g^{-1} with a flat output voltage plateau at around 0.8 V. The bendable and flexible Ca-ion battery with decent voltage output will pave the way for the energy storage devices towards practical applications in flexible and wearable electronics.

KEYWORDS

multivalent metal ion battery, aqueous Ca-ion battery, voltage plateau, In_2O_3 (ITO), flexible and wearable

1 Introduction

Recently, flexible and wearable electronics technologies have received tremendous interest, which posed more rigorous requirements on energy storage with special features of flexibility, bendability, light weight as well as high safety [1, 2]. For the organic media-based Li ion batteries, the safety concern has impeded their widespread usage in security-critical electronic devices despite of their high energy density [3]. In this case, the aqueous battery based on nontoxicity and nonflammability electrolyte is a safer alternative, which also offer tremendous competitiveness in terms of cost, environmental benignity as well as fast charging capability [4–6]. Until now, various types of aqueous battery have gained global research interests with their potential application in flexible electronics markets [7, 8].

Among them, multivalent metal ion battery (Zn^{2+}, Mg^{2+}, Ca^{2+}, Al^{3+}, etc.) is expected to be appealing due to their natural abundance and multi-electron redox capability [9–14]. In particular, Ca-ion battery (CIB) possesses better kinetics than other multivalent ions chemistries in terms of moderate charge density and polarization strength, which would enable faster dynamics in host material [15, 16]. Nevertheless, the development of Ca based battery is still in the preliminary stage because of the limited electrode material to host Ca^{2+} cations [17–20]. As reported, the electrode materials with Ca ions storage capability mainly include prussian blue analogues (CuHCF, NiHCF, BaHCF, etc.) [21–25], transition metal oxides (V_2O_5, Mn_2O_4, WO_3, etc.) [26–28], organic materials [29], etc. Most of the available materials are based on metal-ion intercalation chemistry with layered or tunneled structure, but they still exhibit poor electrochemical performance.

For instance, layered potassium birnessite $K_{0.31}MnO_2{\cdot}0.25H_2O$ has been studied as a host material for intercalating Ca^{2+} cations, whereas obvious capacity decay appears with the capacity drops rapidly from 153 to 78 mAh·g^{-1} for the initial 20 cycles, which was mainly related to the instability of the host material as well as the poor kinetics by solid state diffusion [30]. Meanwhile, it is noteworthy that all of the as-reported aqueous Ca ion batteries just delivered sloping discharge profiles which provide inconsistent working voltage output [17, 31, 32]. A flat discharge platform is rather essential in the practical application due to resulted high and stable energy output, which can also simplify the voltage regulation procedure [33, 34]. Hence, the exploration of suitable host electrodes with excellent Ca storage capability as well as consistent output voltage is worth anticipating for the future application of aqueous Ca ion battery.

In this work, transition metal oxide Sn-doped In_2O_3 (ITO) has been explored as the aqueous CIB anode, which could deliver a high discharge capacity of 71.2 mAh·g^{-1} with ultra-flat

Address correspondence to yanhuanglib@hit.edu.cn

discharge voltage plateau. The Ca storage mechanism of ITO anode has also been revealed based on *ex-situ* X-ray diffraction (XRD), X-ray photoelectron spectroscopy (XPS), and transmission electron microscopy (TEM) characterizations. A flexible aqueous CIB was subsequently assembled with zinc hexacyanoferrate (ZnHCF) cathode and ITO anode sandwiched by polyacrylamide (PAM) hydrogel electrolyte, which delivered a high specific capacity of 75.3 mAh·g^{-1} at 0.4 A·g^{-1}. Remarkably, the CIB exhibits a flat voltage plateau at around 0.8 V with the advantage of providing stable and consistent voltage output. Besides, the CIB exhibits good mechanical flexibility with stable performance under various bending angles. We believe the flexible CIB with stable output voltage will pave the way for the energy storage devices towards practical applications in flexible and wearable electronics.

2 Experimental section

2.1 Preparation of electrode materials and electrolyte

The Sn doped In_2O_3 film was obtained by multitarget magnetron sputtering technique with In (99.99 wt.%) and Sn (99.99 wt.%) targets sputtered onto the substrates. The deposition chamber was evacuated to a base pressure below 5×10^{-6} Pa, which was then maintained at a pressure of 100 Pa with the introduction of 100% pure Ar gas, where the In and Sn targets were sputtered at a radio frequency power of 40 kW. Meanwhile, the substrates were shifted linearly at a rate of 1 m·min^{-1} during the deposition process for spatial uniformity.

The ZnHCF cathode material was prepared by high-temperature coprecipitation [35]. Typically, 100 mL of 0.1 M $ZnSO_4$ and 0.05 M $K_3Fe(CN)_6$ aqueous solution was added dropwisely into 50 mL Deionized (DI) water with continuous stirring. After sufficient reaction at 60 °C, the obtained precipitates were centrifuged for several times with DI water to remove the residues, which were then placed in a vacuum oven and dried at 80 °C for 24 h.

The PAM polymer hydrogel electrolyte was prepared by *in-situ* free radical polymerization. Typically, 2 g gelatin was added into 20 mL 1 M $CaCl_2$ solution and stirred slowly at 80 °C until totally dissolved. Then, 30 mg potassium persulfate (initiator) was added and dissolved. After cooling down, 3 g acrylamide and 3 mg N,N-methylenebisacrylamide (cross-linker) were added into the mixture solution sequentially, which were then stirred for 2 h at 40 °C for grafting reaction. Then the above solution was injected into a mold containing a tiled polyester membrane and polymerized at 60 °C in a vacuum oven for 180 min.

2.2 Materials characterization

XRD measurement was performed under a Bruker D2 Phaser diffractometer with Cu Kα irradiation (λ = 1.54 Å). XPS spectra were collected by an ESCALAB 250 photoelectron spectrometer (Thermo Fisher Scientific) using Al Kα X-ray beam (1,486.6 eV), with charge corrected to the standard C 1s peak at 284.6 eV. Morphology and microstructure characterization was carried out by a field-emission scanning electron microscope (FE-SEM, FEI/Philips XL30) and a field TEM (JEM 2100, 200 kV). The element composition was analyzed by inductively coupled plasma emission spectrometer (ICP).

2.3 Electrodes preparation and cell assembly

The flexible cathode electrodes were prepared by pasting the mixture slurry consisted of the active material (ZnHCF), conductive agent (Super P) and binder (polyvinylidene fluoride, PVDF) (mass ratio of 8:1:1) with N-methyl pyrrolidone (NMP) as solvent onto the carbon cloth, which were then dried in a vacuum oven at 80 °C for 10 h. The flexible ITO anode was obtained by magnetron sputtering onto flexible poly(ethylene terephthalate) (PET) substrates. The flexible CIB was acquired by sandwiching the cathode and anode with the PAM hydrogel electrolyte. The patterned ITO electrode was obtained by corrosion technology, and then the ZnHCF suspension was sprayed onto one side of the electrode with a mask covered on the other ITO side. Finally, a patterned CIB was obtained with a piece of PAM hydrogel electrolyte covered onto the patterned electrode. Prior to cell assembly, the ZnHCF cathode was calcified by discharging to 0.3 V (vs. Ag/AgCl) in $CaCl_2$ solution at a current density of 30 mA·g^{-1}. The active materials mass loading of ZnHCF was around 0.8 mg·cm^{-2}, and the ITO anode mass loading was around 30 μg·cm^{-2}.

2.4 Electrochemical test

Cyclic voltammetry (CV) and galvanostatic charge/discharge (GCD) curves were obtained by an electrochemical workstation (CHI 760e). Galvanostatic charge/discharge cycle measurements were conducted by a LandCT 2001A battery testing system. Electrochemical performance of ITO anode and ZnHCF cathode in 1 M $CaCl_2$ aqueous solution was investigated with a three-electrode configuration where a Pt sheet and an Ag/AgCl electrode were employed as counter and reference electrode, respectively. The specification of Ag/AgCl reference electrode adopted 3 M KCl solution.

3 Results and discussion

The crystalline structure of ITO was analyzed by XRD pattern and presented in Fig. 1(a). All the diffraction peaks were well-indexed to cubic-structured In_2O_3 crystalline (JCPDS No. 71-2194) with no other phase presented. The diffraction peaks labeled by asterisk were derived from the substrate. The strong diffraction peak at 2θ of 30.5° with a few minor peaks at 21.4° and 35.5° were corresponded to the (222), (211), and (400) planes of In_2O_3 phase, respectively. The corresponding illustration of flexible ITO film with cubic crystal structure is shown in Fig. 1(b). Meanwhile, high-resolution TEM (HRTEM) characterization of ITO and the corresponding selected area electron diffraction pattern (SAED) are shown in Fig. 1(c). It can be found that the interfringe spacings of 0.298 nm were matching well with the (222) crystal plane of cubic In_2O_3, which were also in good agreement with the XRD result. The In 3d core-level XPS spectra are shown in Fig. 1(d) (left), which were deconvoluted into spin-orbit doublets $3d_{5/2}$ (444.9 eV) and $3d_{3/2}$ (452.5 eV) of In^{3+} (In_2O_3), respectively, with a peak-to-peak parting of 7.6 eV [36]. In the O 1s core-level spectra as shown in Fig. 1(d) (right), the peaks at 530.3 and 532.0 eV are recognized as the metal-oxygen-metal (In-O-In) lattice feature and surface O species, respectively [37].

The electrochemical behavior of ITO anode was investigated in a three-electrode system with 1 M $CaCl_2$ solution as electrolyte, Pt plate and Ag/AgCl as counter electrode and reference electrode, respectively. The CV profiles of ITO anode at sweep rates ranging from 1 to 20 mV·s^{-1} in the potential window of −0.5–0.5 V (vs. Ag/AgCl) are provided in Fig. 2(a). As shown, one pair of well-defined redox peaks located at around −0.1/0.1 V (vs. Ag/AgCl) were detected, which might be related to the reduction/oxidation reaction of In^{3+}/In redox couple. Further, the detailed electrochemical charge storage mechanism of ITO anode was investigated based on the power law relationship between peak current (i) and scan rate (v)

$$i = av^b \quad (1)$$

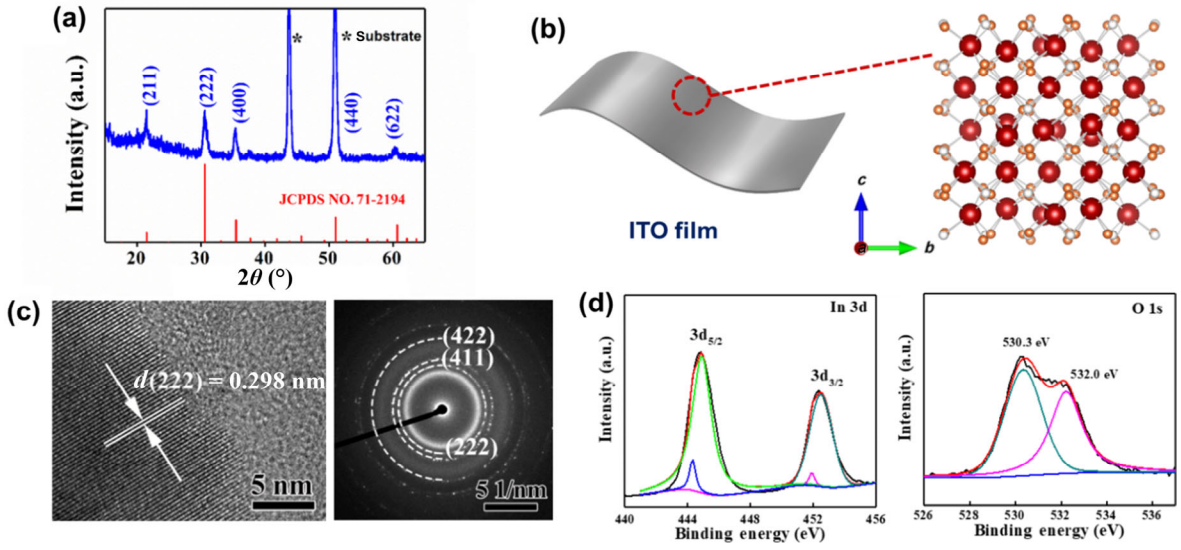

Figure 1 Physical characterization of ITO electrode: (a) XRD pattern of ITO electrode. (b) Illustration of the flexible ITO film with cubic crystal structure. (c) HRTEM image (left) and SAED pattern (right) for ITO. (d) The In 3d and O 1s XPS spectra of ITO.

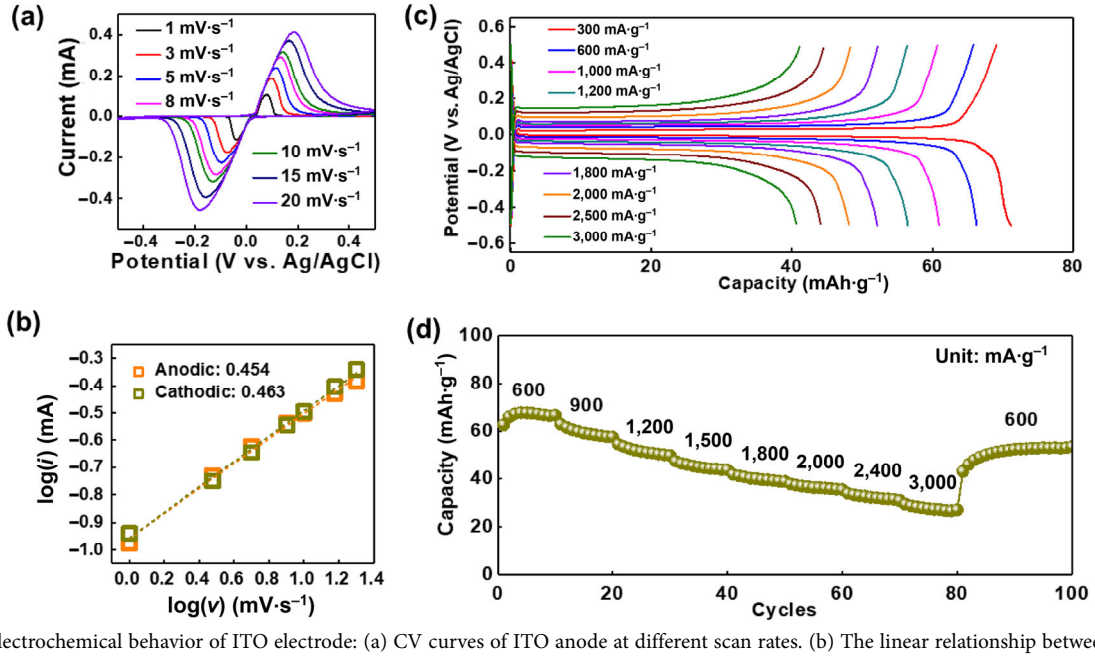

Figure 2 Electrochemical behavior of ITO electrode: (a) CV curves of ITO anode at different scan rates. (b) The linear relationship between log(*i*) and log(*v*). (c) GCD curves of ITO anode at different current densities. (d) Rate capability of ITO anode at different current densities.

where the *b* value was obtained by the slope of the log(*v*)-log(*i*) plots, as shown in Fig. 2(b). The *b* value of 0.5 indicates a total ion diffusion controlled process, and *b* = 1.0 indicates a total capacitive behaviour [38]. Herein, the *b* values for anodic and cathodic process were calculated to be 0.454 and 0.463, respectively, suggesting that the electrochemical reactions process of ITO anode was most determined by the diffusion procedure. Figure 2(c) displays the charge/discharge profiles of the ITO electrode at various current densities ranging from 300 to 3,000 mA·g^{-1}. The ITO electrode could deliver a high capacity of 71.2 and 40.6 mAh·g^{-1} at the current density of 300 and 3,000 mA·g^{-1}, respectively. It is worth highlighting all of the profiles demonstrate super flat charging and discharging plateaus at around 0 V (vs. Ag/AgCl), which pose great advantage for the full battery with consistent voltage and energy output in practical application. Meanwhile, the rate capability of ITO anode at different current densities is provided in Fig. 2(d). As shown, the ITO anode exhibited excellent rate capability with a high capacity of 67.6 mAh·g^{-1} delivered at the current density of 600 mA·g^{-1}. Even at a higher current density of 3,000 mA·g^{-1}, a capacity of 27.5 mAh·g^{-1} was still obtained, which could also return back to 53.4 mAh·g^{-1} when the current density returned to 600 mA·g^{-1}. The cycle performance at current density of 500 mA·g^{-1} was also studied in Fig. S1 in the Electronic Supplementary Material (ESM), which experienced an activation procedure with the capacity increasing gradually to 66.4 mAh·g^{-1} during the first 20 cycles. In the subsequent cycles, slight capacity decrease was observed, which might be ascribed to the attenuation in electrical conductivity of ITO anode upon repeated charge/discharge cycles.

Further, the Ca storage mechanism of ITO electrode was investigated by *ex-situ* characterizations including XPS, XRD, and TEM. Different charge/discharge states marked as A–G points were collected for analysis (Fig. 3(a)). As shown in Fig. 3(b), the characteristic peaks appeared at 347.4 and 351.0 eV, corresponding to Ca $2p_{3/2}$ and Ca $2p_{1/2}$, respectively, were detected at fully discharge state points A and G, suggesting that Ca-related compound were formed during the discharge

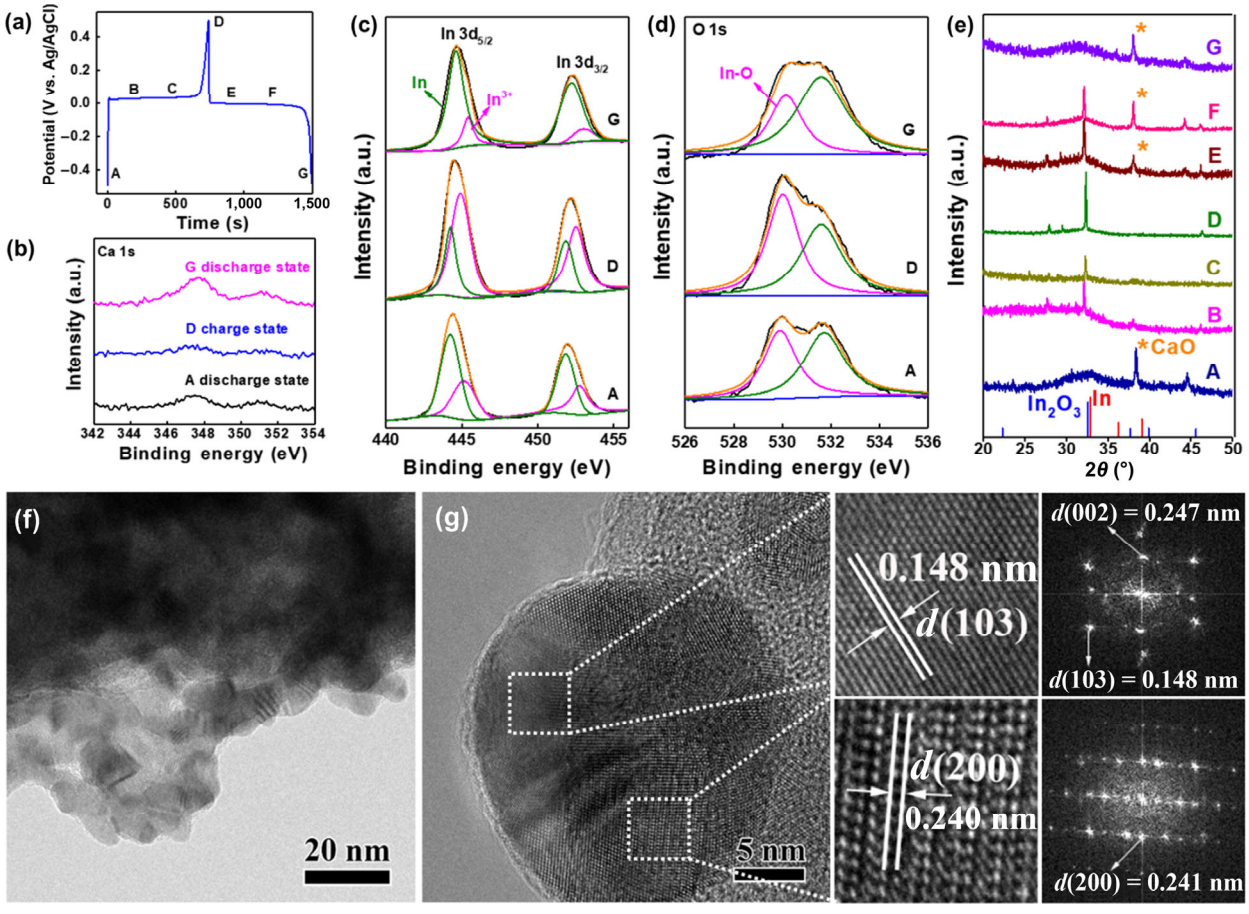

Figure 3 The electrochemical mechanism and structural evolution of ITO electrode during the electrochemical process: (a) The typical charge/discharge curves of electrode in 1 M $CaCl_2$ aqueous electrolyte at a current density of 1 $A{\cdot}g^{-1}$, where the points A–G mark the states collected for analysis. (b) XPS spectra of Ca 1s at fully charge and discharge states. XPS spectra of (c) In 3d and (d) O 1s at fully charge and discharge states. (e) *Ex*-XRD patterns at selected states during charge and discharge process. (f) TEM image of ITO electrode at fully discharge state. (g) HRTEM image at fully discharge state with amplified regions and the corresponding Fourier transform patterns.

process. As observed, the Ca 2p peak almost disappeared at fully charge point D, implying the reversible Ca storage mechanism in ITO electrode. Meanwhile, the In 3d spectra at fully discharge and charge states are provided in Fig. 3(c), which display two peaks located at 444.4 and 452.0 eV, corresponding to In $3d_{3/2}$ and In $3d_{5/2}$, respectively. Notably, the In 3d core peak can be deconvoluted into two components related to In (metallic indium) and In^{3+} (indium oxide), which located at around 444.2, 451.9, 445.3, and 452.6 eV, respectively [37]. At the fully discharge state A, the intensity ratio of InO peak to the In^{3+} peak was calculated to be 1.4. The appearance of InO indicates the reduction of In^{3+} with the introduction of Ca cation due to charge balance, which was similar with the lithium ion battery system [39]. When it was fully charged to 0.5 V (D point), the intensity ratio of In/In^{3+} decreased to 1.1, implying the reversible conversion of In to In^{3+} during charging. Additionally, the SnO_2 component content was confirmed by ICP with the mass weight ratio of SnO_2:In_2O_3 at around 1:10.3. The role of SnO_2 during charge/discharge process was also investigated by XPS as shown in Fig. S2 in the ESM. The Sn $3d_{5/2}$ peak was located at 494.79 eV and the Sn $3d_{3/2}$ peak at 486.33 eV. There was no peak position shifted and no new peak appeared at the fully discharge state (points A and G) and fully charge state (point H), suggesting that the SnO_2 might not participate in the electrochemical redox reaction.

The deconvoluted O 1s core-level peaks at fully charge and discharge state are presented in Fig. 3(d). The two binding energy peaks, located at 530.1 and 531.6 eV, can be assigned to the characteristic bands of oxygen in the In-O lattice and surface bound water, respectively. At the discharging state A, the relative content ratio of lattice oxygen species to surface adsorbed oxygen was calculated to be 0.87, which increased to 1.1 upon charging, proving the reversible formation of In-O lattice with the escape of Ca cation. During the subsequent discharge process, the content ratio of lattice oxygen species decreased to 0.52, further demonstrating the reduction of In_2O_3 to In^0 during discharging with the decrease of oxygen in the In-O lattice.

The structural transition of ITO electrode during charge/discharge process was also investigated by XRD and shown in Fig. 3(e). At fully discharge state point A, there was no obvious diffraction peak of In_2O_3 whereas a small characteristic peak of CaO located at 38.1° was found, suggesting that CaO might be formed during the discharge process. When the ITO electrode was recharged to 0.5 V, the characteristic diffraction peak of In_2O_3 phases located at around 32.6° was found obviously upon Ca^{2+} removal, suggesting the reversible Ca insertion/extraction reaction accompanied with the formation of hexagonal In_2O_3 phase during the charge/discharge process. Further, the disappearance of In_2O_3 characteristic peak during the subsequent discharge process (point G) indicated the reversible phase transformation accompanying the insertion/extraction of Ca ions. Further, HRTEM characterization was employed to disclose the discharge products of ITO electrode upon Ca^{2+} insertion. When the ITO electrode discharged to −0.5 V, numerous nanoparticle aggregates with nanosizes of 5–20 nm were

observed (Fig. 3(f)). In the HRTEM image (Fig. 3(g)), there were two lattices with the interfringe spacings of 0.148 and 0.240 nm observed, matching well with the (103) and (200) crystal planes of tetragonal In (JCPDS No. 85-1409) and cubic CaO phases (JCPDS No. 74-1226), revealing the formation of In and CaO products at discharge state, which are well consistent with the XRD analysis.

In this work, a flexible aqueous CIB was assembled with the zinc hexacyanoferrate (ZnHCF) cathode and ITO anode sandwiched by flexible PAM electrolyte as illustrated in Fig. 4(a). The crystal structure of ZnHCF synthesized by the coprecipitation route was evaluated by XRD (Fig. S3(a) in the ESM), which is consistent with the crystal structure of rhombohedral $Zn_3[Fe(CN)_6]_2$ with the space group of *R-3c* (JCPDS No. 38-0688) [40]. The resulted products displayed irregular nanoparticle morphology as shown in Fig. S3(b) in the ESM. Meanwhile, the Ca^{2+} intercalation/deintercalation behaviour of ZnHCF cathode was investigated by CV and charge/discharge test in a three-electrode system. As shown in Fig. S4(a) in the ESM, one pair of redox peaks located at around 0.61/0.74 V (vs. Ag/AgCl) were observed clearly under different scan rates of 5–20 mV·s^{-1}, corresponding to the reduction/oxidation process of $Zn_3[Fe(III)(CN)_6]_2/Zn_3[Fe(II)(CN)_6]_2$ accompanied by the Ca ion insertion/extraction in PBA framework. Impressively, the CV curves displayed similar shapes and slight peak shifts even at a high scan rate of 20 mV·s^{-1}, suggesting the fast electrochemical redox reaction upon Ca ion intercalation/deintercalation. The corresponding GCD profiles of ZnHCF cathode under different current density are provided in Fig. S4(b) in the ESM, which could deliver a capacity of 71.4 mAh·g^{-1} under a current density of 200 mA·g^{-1} with a flat discharge plateau at around 0.8 V (vs. Ag/AgCl). The XPS characterization of ZnHCF cathode before and after cycling was carried out and shown in Fig. S5 in the ESM. The detection of Ca element after cycles implied the insertion of Ca^{2+} in ZnHCF framework, and the appearance of Fe^{2+} located at around 708.5 eV at the insertion state suggested the partial reduction of Fe^{3+} to Fe^{2+} with the insertion of Ca^{2+}. Based on the above analysis, it can be concluded that the working principle of aqueous CIB was originated from Ca^{2+} intercalation/de-intercalation at ZnHCF cathode together with the conversion reaction at ITO anode. The working principle illustration of aqueous CIB is presented in Fig. 4(b). The electrochemical processes can thereby be summarized by the following equations

Cathode: $CaZn_3[Fe(II)(CN)_6]_2 \rightleftharpoons Zn_3[Fe(III)(CN)_6]_2 + Ca^{2+} + 2e^-$

Anode: $3Ca^{2+} + 6e^- + In_2O_3 \rightleftharpoons 3CaO + 2In$

The electrochemical performance of aqueous CIB was explored by CV and GCD tests. Figure 4(c) shows the CV curves of the full Ca ion battery at scan rates of 10, 15, and 20 mV·s^{-1}, which exhibit similar shapes with one pair of distinct reduction/oxidization peaks at 0.76/1.0 V. The charge/discharge curves of the as-assembled full battery at different current densities are shown in Fig. 4(d). The battery system delivered a specific capacity of 75.3 and 40.1 mAh·g^{-1} (based on the total mass of ITO anode) at current density of 0.4 and 2.2 A·g^{-1}, respectively. It is worth noting that the CIB exhibited an ultra-flat discharge plateau of nearly 0.8 V, which possessed superiority in practical application with consistent high energy output [11, 47]. The low discharging plateau at about 0.2 V might be originated from the Zn deposition on the anode due to the small quantity of Zn^{2+} contained in the electrolyte, which came from ZnHCF cathode during the charge/discharge process. Additionally, the full CIB demonstrated promising rate performance. As shown in Fig. 4(e), the capacity of CIBs could reach 53.6 mAh·g^{-1} at a current density of 700 mA·g^{-1}, which remained at 27.6 mAh·g^{-1} even at a high current density of 3.5 A·g^{-1}. Herein, a slight capacity increase at current density of 0.7 A·g^{-1} was mainly due to the activation process in ITO anode that derived from electrochemical doping, which was a typical n-type semiconductor, and charge carrier concentration would increase with improved electronic conductivity when foreign alkaline-earth Ca^{2+} inserted. The coulombic efficiency also increased with the cycle numbers, which was attributed to the excessively low initial charge capacity of around 4.4 mAh·g^{-1} since the charge carrier migration generated in an instant time when electrochemical doping occurred. Thus, a minor difference in charge/discharge capacity would result in the increase of coulumbic efficiency. When the capacity increased to around 60 mAh·g^{-1} after the initial 20 cycles, the coulombic efficiency could be maintained at around 97.5% during the subsequent cycles. The charge/discharge profiles of the CIBs at the 50th, 80th, 100th, 150th, and 200th cycles under the

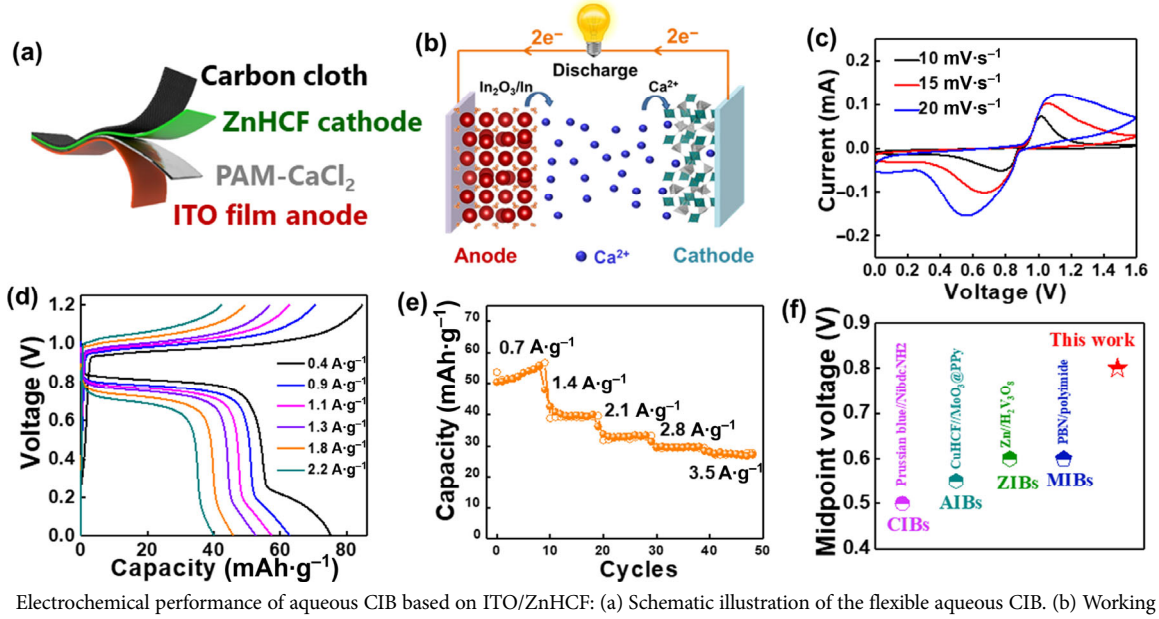

Figure 4 Electrochemical performance of aqueous CIB based on ITO/ZnHCF: (a) Schematic illustration of the flexible aqueous CIB. (b) Working principle schematic of aqueous CIB. (c) CV curves of the solid-state CIB at different scan rates. (d) GCD profiles of CIBs at different current densities. (e) Rate capability of the CIB at various current densities. (f) Comparison of the discharge midpoint voltage with reported aqueous multivalent metal ion batteries.

current density of 500 mA·g^{-1} are provided in Fig. S6(a) in the ESM, demonstrating the stable output performance with small electrode polarization. The cycling stability of CIB is provided in Fig. S6(b) in the ESM with the charge/discharge profiles during the cycling process shown in the inset. As shown, the battery suffered from an activation process with a high capacity of 50.9 mAh·g^{-1} delivered after 200 charge/discharge cycles. The following gradual capacity decay might be derived from the decreased conductivity in electrode materials upon repeated charging/discharging processes. Moreover, we also compared the mid-point voltage of this CIB with other reported aqueous battery systems in Fig. 4(f) [10]. As shown, our CIB offered a relatively high midpoint discharge voltage of 0.8 V. The discharge voltage of some claimed aqueous Al-ion or Mg-ion batteries was relatively low since most of them exhibited sloping or tilting discharge profiles with no obvious voltage plateau [41, 42]. Overall, our CIB with encouraging rate capability and decent voltage output was potentially competitive in stable energy storage application.

Meanwhile, a piece of flexible patterned CIB paper could be fabricated, as shown in Fig. 5(a), which consisted of 16 interdigitated electrodes (eight positive and eight negative electrodes). The length and width of the single electrode were 4.5 and 2.5 mm, respectively, and the gap between the two electrodes was 1.5 mm. The CV curve of the patterned CIB is provided in Fig. 5(b), where a distinct pair of redox peak was observed obviously at 10 mV·s^{-1}. Inset is the digital photograph of an as-fabricated patterned CIB. The flexible solid-state CIBs can be bent at different angles, which had minor effect on the electrochemical performance with well-defined charge/discharge curves maintained as shown in Fig. 5(c). The voltage or current can be increased by connecting multiple CIBs in series or in parallel. As shown in Figs. 5(d) and 5(e), three aqueous CIBs connected in series can yield a stable discharge output voltage of 2.0 V, and three CIBs in parallel could deliver a capacity three times higher than that of a single battery. As a demonstration, two CIBs connected in series, no matter in flat or bent state, were sufficient to light up an electronic watch as shown in Fig. 5(f), showing great application potential in flexible and wearable electronics.

4 Conclusions

In this work, transition metal oxide ITO has been explored as the aqueous CIB anode, which could deliver a high discharge capacity of 71.2 mAh·g^{-1} with an ultra-flat discharge voltage plateau. Based on *ex-situ* XRD, XPS, and TEM characterizations, the Ca ion involved reversible conversion reaction is revealed to account for the Ca storage mechanism, which is different from all previously reported electrode materials for CIB. A flexible aqueous CIB was subsequently assembled by utilizing cathode and ITO anode sandwiched by a solid-state hydrogel PAM electrolyte, which delivered a high specific capacity of 75.3 mAh·g^{-1} at 0.4 A·g^{-1}. It is worth mentioning that the aqueous CIB also possesses an ultraflat high output voltage plateau of nearly 0.8 V, providing stable and consistent high energy output. Besides, the aqueous CIB is flexible and bendable with stable performance under various bending angles. We believe the flexible CIB in our work will pave the way for the energy storage devices towards practical applications in flexible and wearable electronics with stable high output voltage and energy.

Acknowledgements

This research was supported by the National Natural Science Foundation of China (No. 21805063), the Natural Science Foundation of Guangdong Province for Distinguished Young Scholars (No. 2018B030306022), the Project of International Science and Technology Cooperation in Guangdong Province (No. 2020A0505100016), and the Shenzhen Sauvage Nobel Laureate Laboratory for Smart Materials and Research Innovation Fund of Harbin Institute of Technology (No. HIT.NSRIF. 2020063). The authors also acknowledge the support from the China Postdoctoral Science Foundation (No. 2018M641823).

Electronic Supplementary Material: Supplementary material (cycling performance of ITO anode and CIBs, physical characterization, and charge/discharge behavior of ZnHCF cathode) is available in the online version of this article at https://doi.org/10.1007/s12274-021-3550-5.

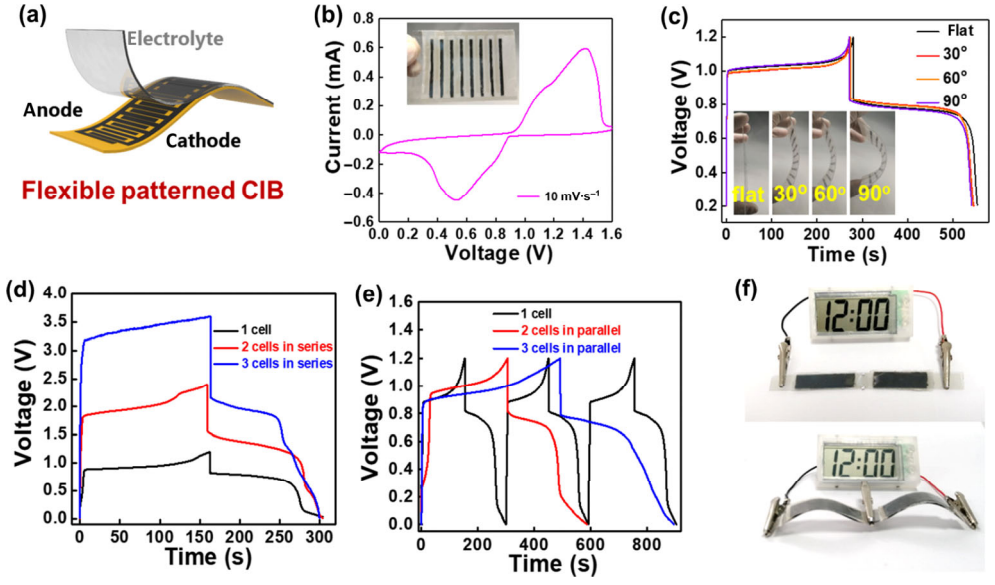

Figure 5 Demonstration of the flexible CIB: (a) Schematic of the flexible patterned CIB. (b) The CV curve of the patterned CIB (inset is the photograph of patterned Ca ion full cell). (c) GCD curve of the flexible CIB at different bending angles. (d) Charge/discharge curves of one, two, and three batteries in series. (e) Charge/discharge curves of one, two, and three batteries in parallel. (f) Two CIBs connected in series could power an electronic watch under flat or bending state.

References

[1] Li, C. W.; Zhang, Q. C.; Sun, J.; Li, T. T.; E, S. F.; Zhu, Z. Z.; He, B.; Zhou, Z. Y.; Li, Q. L.; Yao, Y. G. High-performance quasi-solid-state flexible aqueous rechargeable Ag-Zn battery based on metal–organic framework-derived Ag nanowires. *ACS Energy Lett*. **2018**, *3*, 2761–2768.

[2] Li, H. F.; Tang, Z. J.; Liu, Z. X.; Zhi, C. Y. Evaluating flexibility and wearability of flexible energy storage devices. *Joule* **2019**, *3*, 613–619.

[3] Liu, Z. X.; Li, H. F.; Zhu, M. S.; Huang, Y.; Tang, Z. J.; Pei, Z. X.; Wang, Z. F.; Shi, Z. C.; Liu, J.; Huang, Y. et al. Towards wearable electronic devices: A quasi-solid-state aqueous lithium-ion battery with outstanding stability, flexibility, safety and breathability. *Nano Energy* **2018**, *44*, 164–173.

[4] Zhang, L. Y.; Chen, L.; Zhou, X. F.; Liu, Z. P. Towards high-voltage aqueous metal-ion batteries beyond 1.5 V: The zinc/zinc hexacyanoferrate system. *Adv. Energy Mater*. **2015**, *5*, 1400930.

[5] Chao, D. L.; Zhou, W. H.; Xie, F. X.; Ye, C.; Li, H.; Jaroniec, M.; Qiao, S. Z. Roadmap for advanced aqueous batteries: From design of materials to applications. *Sci. Adv*. **2020**, *6*, eaba4098.

[6] Yang, W. H.; Du, X. F.; Zhao, J. W.; Chen, Z.; Li, J. J.; Xie, J.; Zhang, Y. J.; Cui, Z. L.; Kong, Q. Y.; Zhao, Z. M. et al. Hydrated eutectic electrolytes with ligand-oriented solvation shells for long-cycling zinc-organic batteries. *Joule* **2020**, *4*, 1557–1574.

[7] Ma, L. T.; Chen, S. M.; Long, C. B.; Li, X. L.; Zhao, Y. W.; Liu, Z. X.; Huang, Z. D.; Dong, B. B.; Zapien, J. A.; Zhi, C. Y. Achieving high-voltage and high-capacity aqueous rechargeable zinc ion battery by incorporating two-species redox reaction. *Adv. Energy Mater*. **2019**, *9*, 1902446.

[8] Xie, J.; Yu, F.; Zhao, J. W.; Guo, W.; Zhang, H. L.; Cui, G. L.; Zhang, Q. C. An irreversible electrolyte anion-doping strategy toward a superior aqueous Zn-organic battery. *Energy Storage Mater*. **2020**, *33*, 283–289.

[9] Gao, Y. N.; Yang, H. Y.; Wang, X. R.; Bai, Y.; Zhu, N.; Guo, S. N.; Suo, L. M.; Li, H.; Xu, H. J.; Wu, C. The compensation effect mechanism of Fe-Ni mixed prussian blue analogues in aqueous rechargeable aluminum-ion batteries. *ChemSusChem* **2020**, *13*, 732–740.

[10] Adil, M.; Sarkar, A.; Roy, A.; Panda, M. R.; Nagendra, A.; Mitra, S. Practical aqueous calcium-ion battery full-cells for future stationary storage. *ACS Appl. Mater. Interfaces* **2020**, *12*, 11489–11503.

[11] Wang, F.; Fan, X. L.; Gao, T.; Sun, W.; Ma, Z. H.; Yang, C. Y.; Han, F. D.; Xu, K.; Wang, C. S. High-voltage aqueous magnesium ion batteries. *ACS Cent. Sci*. **2017**, *3*, 1121–1128.

[12] Wang, P. P.; Chen, Z.; Wang, H.; Ji, Z. Y.; Feng, Y. P.; Wang, J. Q.; Liu, J.; Hu, M. M.; Fei, J. B.; Gan, W. et al. A high-performance flexible aqueous Al ion rechargeable battery with long cycle life. *Energy Storage Mater*. **2020**, *25*, 426–435.

[13] Li, Z. Y.; Vinayan, B. P.; Jankowski, P.; Njel, C.; Roy, A.; Vegge, T.; Maibach, J.; Lastra, J. M. G.; Fichtner, M.; Zhao-Karger, Z. Multi-electron reactions enabled by anion-based redox chemistry for high-energy multivalent rechargeable batteries. *Angew. Chem., Int. Ed*. **2020**, *59*, 11483–11490.

[14] Ma, L. T.; Li, X. L.; Zhang, G. B.; Huang, Z. D.; Han, C. P.; Li, H. F.; Tang, Z. J.; Zhi, C. Y. Initiating a wearable solid-state Mg hybrid ion full battery with high voltage, high capacity and ultra-long lifespan in air. *Energy Storage Mater*. **2020**, *31*, 451–458.

[15] Ponrouch, A.; Frontera, C.; Bardé, F.; Palacín, M. R. Towards a calcium-based rechargeable battery. *Nat. Mater*. **2016**, *15*, 169–172.

[16] Wang, M.; Jiang, C. L.; Zhang, S. Q.; Song, X. H.; Tang, Y. B.; Cheng, H. M. Reversible calcium alloying enables a practical room-temperature rechargeable calcium-ion battery with a high discharge voltage. *Nat. Chem*. **2018**, *10*, 667–672.

[17] Wu, N. Z.; Yao, W. J.; Song, X. H.; Zhang, G.; Chen, B. J.; Yang, J. H.; Tang, Y. B. A calcium-ion hybrid energy storage device with high capacity and long cycling life under room temperature. *Adv. Energy Mater*. **2019**, *9*, 1803865.

[18] Arroyo-de Dompablo, M. E.; Ponrouch, A.; Johansson, P.; Palacín, M. R. Achievements, challenges, and prospects of calcium batteries. *Chem. Rev*. **2020**, *120*, 6331–6357.

[19] Lang, J. H.; Jiang, C. L.; Fang, Y.; Shi, L.; Miao, S. J.; Tang, Y. B. Room-temperature rechargeable Ca-ion based hybrid batteries with high rate capability and long-term cycling life. *Adv. Energy Mater*. **2019**, *9*, 1901099.

[20] Ji, B. F.; He, H. Y.; Yao, W. J.; Tang, Y. B. Recent advances and perspectives on calcium-ion storage: Key materials and devices. *Adv. Mater*. **2021**, *33*, 2005501.

[21] Vo, T. N.; Hur, J.; Kim, I. T. Enabling high performance calcium-ion batteries from prussian blue and metal-organic compound materials. *ACS Sustain. Chem. Eng*. **2020**, *8*, 2596–2601.

[22] Adil, M.; Dutta, P. K.; Mitra, S. An aqueous Ca-ion full cell comprising BaHCF cathode and MCMB anode. *ChemistrySelect* **2018**, *3*, 3687–3690.

[23] Lee, C.; Jeong, S. K. A novel strategy to improve the electroche. mical performance of a prussian blue analogue electrode for calcium-ion batteries. *Electrochemistry* **2018**, *86*, 134–137.

[24] Tojo, T.; Sugiura, Y.; Inada, R.; Sakurai, Y. Reversible calcium ion batteries using a dehydrated prussian blue analogue cathode. *Electrochim. Acta* **2016**, *207*, 22–27.

[25] Kuperman, N.; Padigi, P.; Goncher, G.; Evans, D.; Thiebes, J.; Solanki, R. High performance prussian blue cathode for nonaqueous Ca-ion intercalation battery. *J. Power Sources* **2017**, *342*, 414–418.

[26] Xu, X. M.; Xiong, F. Y.; Meng, J. S.; Wang, X. P.; Niu, C. J.; An, Q. Y.; Mai, L. Q. Vanadium-based nanomaterials: A promising family for emerging metal-ion batteries, *Adv. Funct. Mater*. **2020**, *30*, 1904398.

[27] Nolis, G. M.; Adil, A.; Yoo, H. D.; Hu, L. H.; Bayliss, R. D.; Lapidus, S. H.; Berkland, L.; Phillips, P. J.; Freeland, J. W.; Kim, C. et al. Electrochemical reduction of a spinel-type manganese oxide cathode in aqueous electrolytes with Ca^{2+} or Zn^{2+}. *J. Phys. Chem. C* **2018**, *122*, 4182–4188.

[28] Wang, J. J.; Tan, S. S.; Xiong, F. Y.; Yu, R. H.; Wu, P. J.; Cui, L. M.; An, Q. Y. $VOPO_4{\cdot}2H_2O$ as a new cathode material for rechargeable Ca-ion batteries. *Chem. Commun*. **2020**, *56*, 3805–3808.

[29] Xie, J.; Zhang, Q. C. Recent progress in multivalent metal (Mg, Zn, Ca, and Al) and metal-ion rechargeable batteries with organic materials as promising electrodes. *Small* **2019**, *15*, 1805061.

[30] Hyoung, J.; Heo, J. W.; Hong, S. T. Investigation of electrochemical calcium-ion energy storage mechanism in potassium birnessite. *J. Power Sources* **2018**, *390*, 127–133.

[31] Xu, X. M.; Duan, M. Y.; Yue, Y. F.; Li, Q.; Zhang, X.; Wu, L.; Wu, P. J.; Song, B.; Mai, L. Q. Bilayered $Mg_{0.25}V_2O_5{\cdot}H_2O$ as a stable cathode for rechargeable Ca-ion batteries. *ACS Energy Lett*. **2019**, *4*, 1328–1335.

[32] Liu, Z. X.; Huang, Y.; Huang, Y.; Yang, Q.; Li, X. L.; Huang, Z. D.; Zhi, C. Y. Voltage issue of aqueous rechargeable metal-ion batteries. *Chem. Soc. Rev*. **2020**, *49*, 180–232.

[33] Liu, Z. X.; Yang, Q.; Wang, D. H.; Liang, G. J.; Zhu, Y. H.; Mo, F. N.; Huang, Z. D.; Li, X. L.; Ma, L. T.; Tang, T. C. et al. A flexible solid-state aqueous zinc hybrid battery with flat and high-voltage discharge plateau. *Adv. Energy Mater*. **2019**, *9*, 1902473.

[34] Zhao, Q.; Huang, W. W.; Luo, Z. Q.; Liu, L. J.; Lu, Y.; Li, Y. X.; Li, L.; Hu, J. Y.; Ma, H.; Chen, J. High-capacity aqueous zinc batteries using sustainable quinone electrodes, *Sci. Adv*. **2018**, *4*, eaao1761.

[35] Chen, Z.; Wang, P. P.; Ji, Z. Y.; Wang, H.; Liu, J.; Wang, J. Q.; Hu, M. M.; Huang, Y. High-voltage flexible aqueous Zn-ion battery with extremely low dropout voltage and super-flat platform. *Nano-Micro Lett*. **2020**, *12*, 75.

[36] Alsaif, M. M. Y. A.; Kuriakose, S.; Walia, S.; Syed, N.; Jannat, A.; Zhang, B. Y.; Haque, F.; Mohiuddin, M.; Alkathiri, T.; Pillai, N. et al. 2D SnO/In_2O_3 van der waals heterostructure photodetector based on printed oxide skin of liquid metals. *Adv. Mater. Inter*. **2019**, *6*, 1900007.

[37] Reddy, I. N.; Reddy, C. V.; Cho, M.; Shim, J.; Kim, D. Structural, optical and XPS study of thermal evaporated In_2O_3 thin films. *Mater. Res. Express* **2017**, *4*, 086406.

[38] Lou, S. F.; Cheng, X. Q.; Gao, J. L.; Li, Q.; Wang, L.; Cao, Y.; Ma, Y. L.; Zuo, P. J.; Gao, Y. Z.; Du, C. Y. et al. Pseudocapacitive Li^+ intercalation in porous $Ti_2Nb_{10}O_{29}$ nanospheres enables ultra-fast lithium storage. *Energy Storage Mater*. **2018**, *11*, 57–66.

[39] Ho, W. H.; Li, C. F.; Liu, H. C.; Yen, S. K. Electrochemical performance of In_2O_3 thin film electrode in lithium cell. *J. Power Sources* **2008**, *175*, 897–902.

[40] Niu, L.; Chen, L.; Zhang, J.; Jiang, P.; Liu, Z. P. Revisiting the open-framework zinc hexacyanoferrate: The role of ternary electrolyte and sodium-ion intercalation mechanism. *J. Power Sources* **2018**, *380*, 135–141.

[41] Chen, L.; Bao, J. L.; Dong, X.; Truhlar, D. G.; Wang, Y.; Wang, C.; Xia, Y. Aqueous Mg-ion battery based on polyimide anode and prussian blue cathode. *ACS Energy Lett*. **2017**, *2*, 1115–1121.

[42] Pang, Q.; Sun, C. L.; Yu, Y. H.; Zhao, K. N.; Zhang, Z. Y.; Voyles, P. M.; Chen, G.; Wei, Y. J.; Wang, X. D. $H_2V_3O_8$ nanowire/graphene electrodes for aqueous rechargeable zinc ion batteries with high rate capability and large capacity. *Adv. Energy Mater*. **2018**, *8*, 1800144.